ACS APPLIED ENERGY MATERIALS

www.acsaem.org Article

Phase Transition Induced Enhanced Performance of Sodium-Rich $Na_{1.2}Mn_{0.8}O_{2-y}F_y$ (y = 0–0.5) Cathodes

Bala Krishnan Ganesan and Yun-Sung Lee*

Cite This: *ACS Appl. Energy Mater.* 2023, 6, 960–968 Read Online

ACCESS | Metrics & More | Article Recommendations | Supporting Information

ABSTRACT: Increasing capacity and cycle stability is key to successfully commercializing sodium battery technologies. Currently, cation-rich cathodes are well suited for this trend owing to superior overall performance through fluorine substitution in the cation. However, the exact effects and synergy due to fluorine substitution as anions are still unknown. Understanding such synergistic effects can significantly facilitate increasing the capacity, leading to maximum performance at optimum conditions. In this work, the systematic addition of F into sodium-layered oxide and its corresponding changes in the crystal structure or phase formation are extensively studied. More specifically, the effect of fluorine substitution in the anion site on Na diffusion and the Na–Tm polyhedral are extensively studied using X-ray diffraction and subsequent Rietveld analysis. In addition, the effects of F on transition metals (i.e., Mn) and its valence states are also analyzed using X-ray absorption spectroscopy. $Na_{1.2}Mn_{0.8}O_{1.5}F_{0.5}$ not only showed superior capacity of approximately 172 mAh g^{-1} and capacity retention but also remarkable cycling stability for up to 300 cycles at higher current densities. Improvements in the performance due to distortion induced by F substitution are also presented. This study provides insight into the transition of cathode material properties from F doping (y = 0–0.2) to F substitution ($y \geq 0.3$) and the associated structural changes and capacity improvements.

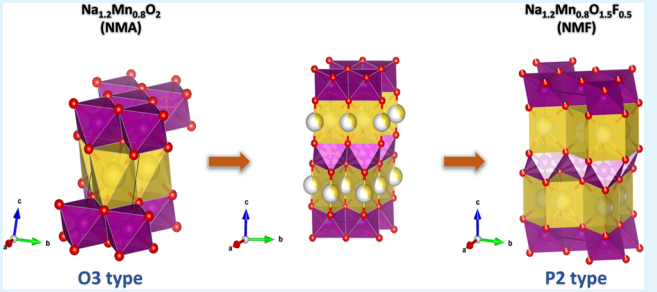

KEYWORDS: *fluorine substitution, sodium-rich cathode, layered oxide cathode, phase transition, sodium ion battery*

INTRODUCTION

With sodium (Na) ion batteries gaining traction as the low-cost lithium (Li) ion battery alternative, the need for efficient cathodes in terms of capacity and cycle life with higher energy density is imminent.[1−6] Higher-energy-density layered cathode materials with Co and Ni in transition-metal sites are now preferred by researchers. However, the exponential increase in demand and inconsistent supply chain act as a bottleneck in achieving higher energy densities. In particular, because cobalt is very expensive, current research is focusing on Mn and Fe as transition metals, which are both low-cost and abundant.[7−9] However, the belief that cathodes must be perfectly layered without defects or distortions before and after cycling greatly restricts the potential of these cathode materials. Recent works on various substitutions, in particular, disordered rock salt (DRX) with anion fluorination, have demonstrated that capacity retention improves upon substituting fluorine for oxygen.[10−13]

Other recent studies have proved that high-energy cathodes can be achieved even with disordered cations, which show higher Li percolation.[11,14−16] These results pave the way for cation-rich cathode materials based on Mn,[17,18] Cr,[19] Ni,[20,21] and Nb.[22,23] In addition, F substitution at the oxygen site further improves the capacity retention and cycle stability by cation valency reduction, suggesting that fluorination is the key to maximizing performance.[10,24] Typically, these cathodes are synthesized by solid-state synthesis and Na–F as the only source of F. However, the dissociation energy of NaF is very high, such that its miscibility into metal oxides is very low when concentration is increased. In the case of cation-disordered rock salt (DRX) structures, fluorine preferentially incorporates into the cation-rich site (such as a Li-rich site), whereas this is severely hindered in ordered rock salt structures.[25] This inability of fluorine to incorporate into the cation-rich site results in the formation of a metal fluoride phase. However, the exact reason behind the improvement in the capacity retention is still unknown, and the limits of fluorination in sodium-rich cathodes are still not clear.

Mn and F are two of the few materials that are inexpensive and highly abundant in the earth's crust that can be used in the development of low-cost next-generation sodium cathode materials. Various $NaMnO_2$ cathode materials have been reported earlier that are well-known for their high-energy

Received: October 18, 2022
Accepted: December 19, 2022
Published: January 6, 2023

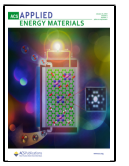

https://doi.org/10.1021/acsaem.2c03391
ACS Appl. Energy Mater. 2023, 6, 960–968

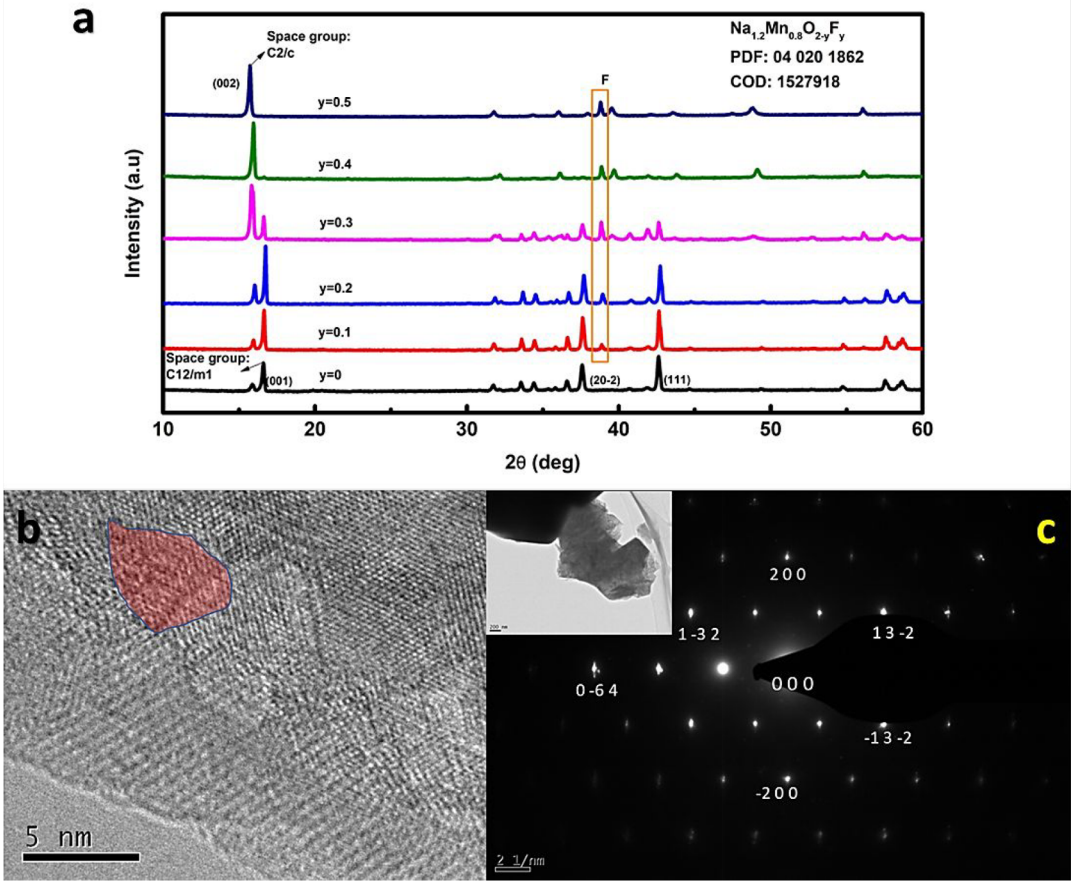

Figure 1. XRD images of the $Na_{1.2}Mn_{0.8}O_{2-y}F_y$ cathode with the increase in F content (a). TEM and SAED pattern of the NMF sample with encircled area highlighting the distortion in ordering (b, c).

densities and safety.[26,27] These $NaMnO_2$ materials consist of several polymorphs, mainly O3 and P2 types, which were first identified and reported by Parant et al. in 1971.[28] These diversities in phases occur due to variations in the Na/Mn ratio during synthesis and associated reaction temperatures. Mn^{3+} as a transition metal is very much susceptible to Jahn−Teller (JT) distortions, which lead to distorted phase formations with multiple variations. In electrochemical processes, a $Mn^{III/IV}$ redox couple is thought to cause large anisotropic volume changes and distortions.[29,30] However, to suppress this anisotropic volume change or distortion, Tm doping is commonly used.

The drastic effects on the performance of $NaMnO_2$ due to Jahn−Teller distortion and the preparation of high-phase purity samples are extensively studied by Kumakura et al.[27] In their study, two similar P2 phases with orthogonal and hexagonal lattices of high purity were achieved by controlling the synthesis temperature and maintaining the Na/Mn ratio. At the end of the study, it was found that in $NaMnO_2$ Jahn−Teller distortions do not deteriorate the reversible Na-ion intercalation, whereas Mn defects were critical in unlocking superior performance in these classes of cathodes. Associated with JT distortions are huge volumetric changes that may hinder the cycle stability of cathode materials, requiring the appropriate modifications. Inspired by the higher capacity of Mn-based Li-rich cathodes, which deliver a very high initial capacity of 200 mAh g^{-1} and superior stability by fluorinated Li-rich cathodes,[17,31] a new class of Na-rich cathodes based on Mn as a transition metal and F as an anion substitute is proposed in this study.

In this paper, fluorine substitution is performed progressively from $y = 0-0.5$ in a high-capacity cathode material in which Mn^{3+}/Mn^{4+} is used as a redox transition metal. Through this systematic substitution, the efficacy of fluorine in improving the capacity and cycle stability, and therefore the improvement in cathode performance, is presented. Combining the Rietveld and XANES methods, distortion caused by fluorine substitution in the crystal structure is systematically analyzed. The changes in phases of pristine Na-rich oxide with the increase in fluorine concentration and its subsequent effect on the overall performance of the cathode are also studied. These analyses are important in validating and evaluating the process of the existing synthesis route. They also clarify the challenges in the process of fabricating high-F-containing cathodes. Results indicate that F substitution achieves Na-rich cathode stability for at least 300 cycles, even at higher current densities, a performance which far exceeds its Li-rich counterparts. However, we postulate that the formation of the NaF phase is inevitable at higher F concentrations due to its preferential attachment.

EXPERIMENTAL SETUP

Synthesis of Na-Rich $Na_{1.2}Mn_{0.8}O_{2-y}F_y$ Samples. Sodium-rich samples were synthesized using the conventional solid-state method, and F was introduced into the structure using NaF. The stoichiometric amount of sodium carbonate (Sigma-Aldrich, >99.5%), manganese(III) oxide (Sigma-Aldrich, 99%), sodium

https://doi.org/10.1021/acsaem.2c03391
ACS Appl. Energy Mater. 2023, 6, 960−968

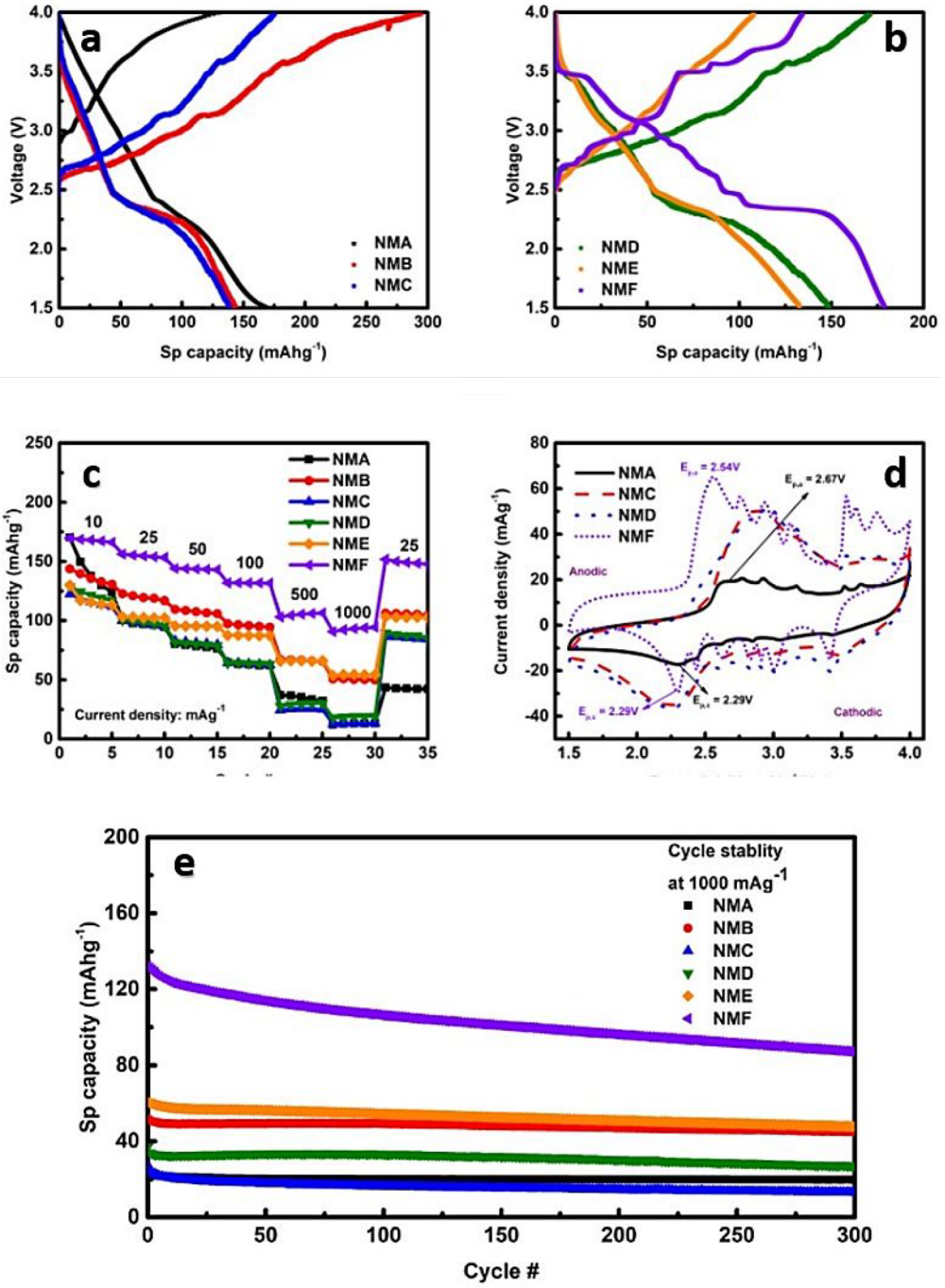

Figure 2. GCD of Na-rich cathode materials with different levels of F substitution (a, b). Rate performance at different current densities (c). Cyclic voltammogram of Na-rich cathodes with different F levels: y = 0.0, 0.2, 0.3, and 0.5 (d). Cycle stability at 1000 mA/g current density (e).

fluoride (Sigma-Aldrich, 99%), and 20 wt % citric acid (Sigma-Aldrich, 99%) were milled for 6 h using acetone as a solvent. Later, the milled precursors were dried in a vacuum oven and pressed into pellets. Samples were heated to 700 °C for 12 h at a heating rate of 5 °C min^{-1} in a muffle furnace and quenched to room temperature in a vacuum atmosphere of a glovebox chamber to yield Na-rich cathodes. To avoid contact with air and moisture, the samples were stored inside the glovebox for future progress. For further use, the samples with various F stoichiometry, i.e., y = 0, 0.1, 0.2, 0.3, 0.4, and 0.5, were labeled as NMA, NMB, NMC, NMD, NME, and NMF, respectively.

Material Characterization. X-ray diffraction is used here for crystal structure characterization (XRD; Cu Kα radiation, Rint 1000, Rigaku, Japan) in the 2θ range of 10°−90°. The texture and other properties such as particle size and surface texture were evaluated using field emission scanning electron microscopy (FE-SEM, S-4700, Hitachi, Japan) coupled with an energy-dispersive X-ray spectroscopy (EDX) module and interlayers using high-resolution transmission electron microscopy (HR-TEM; JEM-2000, EX-II, JEOL, Japan). Oxidation states and coordination chemistry of all the samples were analyzed using XAS analysis (Rigaku RXAS, 3 kW X-ray generator, W target, crystal Ge(220) S-PC(Ar) 1.5″SC REX2000 software) for Mn K-edge spectra.

Electrochemical Measurements. Inside a glovebox, under a controlled atmosphere of ultrapure argon, using CR2032 coin cells, electrochemical studies of all the samples were performed. The cells cathode consisted of the synthesized material and metallic Na as the anode separated by a polypropylene separator, with 1 M $NaPF_6$ in diglyme as the electrolyte. The cathode materials for cell testing were

https://doi.org/10.1021/acsaem.2c03391
ACS Appl. Energy Mater. 2023, 6, 960−968

prepared by mixing 80 mg of conductive carbon and 40 mg of poly(vinylidene difluoride) (PVDF) as binder followed by through mixing of 280 mg of cathode-active material with subsequent NMP addition as solvent. The obtained slurry is coated using the doctor-blade method for 5 mil thickness on aluminum current collector and dried in an oven at 120 °C for 8 h before cell fabrication. Charge–discharge (C–DC) studies were performed for voltage range of 1.5–4.0 V at current rates varying from 0.01 to 1 A g^{-1} using a WonATech battery test system. Cyclic voltammetry and electrochemical impedance spectra (EIS) were conducted using an electrochemical analyzer (SP-150, Biologic, France).

RESULTS AND DISCUSSION

X-ray Diffraction Analysis (XRD). Initially, to determine the structure, XRD was performed on all samples with y = 0–0.5 F molar content (i.e., NMA to NMF) for the range 10°–80°. Figure 1a shows the XRD peaks of the gradual increase in the F content in NMA with the subsequent decrease in oxygen content. With the increase in the F content, it can be observed that the high-intensity peaks shift from 16.6° (2θ) to 15.7° (2θ) with both peaks corresponding to the 002 plane of $NaMnO_2$ but with different lattice structures. In addition, the NaF peaks were also observed in all the F-substituted samples, of which the structural composition was analyzed and is discussed in the Rietveld Analysis section. It is interesting to note that the $Na_{1.2}Mn_{0.8}O_yF_{1-y}$ (NMOF) crystal structure completely changed from one phase to another with the increase in F content. Such a drastic change in crystal structure confirms that F was infused into the system and responsible for changing the crystal structure.

Electron Microscopy. The microstructure and surface textures of the cathode materials were analyzed using electron microscopy. First, in the scanning electron microscope (SEM), it is interesting to analyze that the particles of NMA have become thinner and reduced in size upon F substitution. Though initially, NMA particles were about 3 μm, upon fluorination the particle size was reduced to about 1 μm for NMF. NMF were observed to be blocks of brick-like structures with few patches due to carbon on the surface, as shown in Figure S1. Second, NMF was analyzed using transmission electron microscopy, the images and diffraction patterns of which are shown in Figure 1b,c. Selected area electron diffraction (SAED) was performed on the diffraction pattern, revealing discrete spots representing the highly crystalline nature of the samples. Using the CrysTBox diffraction analysis software,[32,33] the planes corresponding to each diffraction spot were analyzed. Furthermore, using the transmission electron images, the lattice fringes obtained were used to analyze the short- and long-range ordering (SRO and LRO, respectively). A study by Ceder et al.[34] found that SRO is a common phenomenon that occurs in all cathode-rich samples, particularly in Li-rich cathodes. In general, without fluorination, SRO severely hinders cation (Li or Na) diffusion. However, heavy fluorination can modify SRO and improve the capacity of the cathode, a topic which is analyzed in the following sections.

Electrochemical Analysis. To further evaluate the electrochemical performances of samples with various F-content ratios, techniques such as the galvanostatic charge–discharge (GCD) method and cyclic voltammetry (CV), as well as parameters such as rate performance and cycle stability, were analyzed as shown in Figure 2. First, to evaluate the charge storage capacity of the electrode at a given current density, the GCD and rate performance studies were conducted on all samples. In Figure 2a,b, at a given current density of 10 mA/g, the NMF sample demonstrated the highest capacity of 174 mAh g^{-1} followed by NMA with approximately 172 mAh g^{-1}. Among the samples, NMC demonstrated the least capacity of approximately 128 mAh g^{-1}. In addition to capacity, it is interesting to analyze the GCD curve because, unlike many other cathode materials that possess a flat plateau region at approximately half the cell voltage, for the F-substituted samples the GCD is well divided into a multistep process. It is to be noted that for NMF, first charge capacity was about 127 mAh g^{-1}, which corresponds to 0.46 Na^+ per formula unit. Thus, in the first charge this composition act as limiting barrier displaying much lesser charging capacity. Upon subsequent discharge, the structure is recouped with sodium, which is removed in subsequent charge cycle normally and giving higher charging capacity. It is to be noted that GCD features of NMF samples are very much in similar, multistep processes as in P2 $Na_{2/3}MnO_2$. The clear transition from the single-plateau GCD behavior in NMA into a multistep process in NMF is clearly visible in Figure 2b. The reason behind the multistep GCD process is explained in the following sections. Although in general applications this multistep GCD process is not desirable, its capacity output is convincingly high enough to render NMF a better candidate.

The rate performance of all samples was analyzed by increasing the current density from 10 to 1000 mA g^{-1} stepwise, as shown in Figure 2c. The rate performance analysis better evaluates the capacity at different current rates and the cathode diffusion kinetics at higher current rates. NMF outperformed all the samples by demonstrating a high-rate capability. When the current rate increased from 10 to 1000 mA g^{-1}, the capacity dropped from 174 to 110 mAh g^{-1}. However, the capacity of the pristine sample without F dropped from 172 mAh g^{-1} to a mere 12 mAh g^{-1}, indicating a poor rate performance due to sluggish cathode kinetics. The samples were further cycled at a current density of 1000 mA g^{-1} to evaluate the stability in long-term cycling, as shown in Figure 2e. Again, NMF outperformed all the samples in terms of capacity along with cycle stability for 300 cycles with a capacity retention of more than 68%. Although this capacity fade is not on par with that of commercial standards, it is to be noted that compared with the pristine NMA sample the cycle stability is more stable with the F-substituted samples throughout the cycling process. As reported previously,[35] in oxide electrodes, the capacity fade is mainly associated with spinel formation, whereas, in the case of the F-substituted samples, the oxygen loss is reduced and structural stability is significantly improved with the presence of F, greatly reinforcing the structure. To verify the same, NMA and NMF samples were analyzed in SEM postcycling, and the NMF sample was observed to be intact after cycling as shown in Figure S8.

To better understand the multistep GCD process, CV was analyzed for all the samples with increasing order of F substitution. In Figure 2d, the CV of samples NMA, NMC, NMD, and NMF with F levels of y = 0, 0.2, 0.3, and 0.5, respectively, were compared to better understand the evolution of the redox peaks with the increase in F content. The redox peak potential during the cathodic and anodic sweeps is represented as $E_{p,c}$ and $E_{p,a}$, respectively. According to the Nernst equation, an ideal system should maintain a peak separation difference of approximately 57 mV. However, in reality, a system that has a redox peak difference close to this

https://doi.org/10.1021/acsaem.2c03391
ACS Appl. Energy Mater. 2023, 6, 960–968

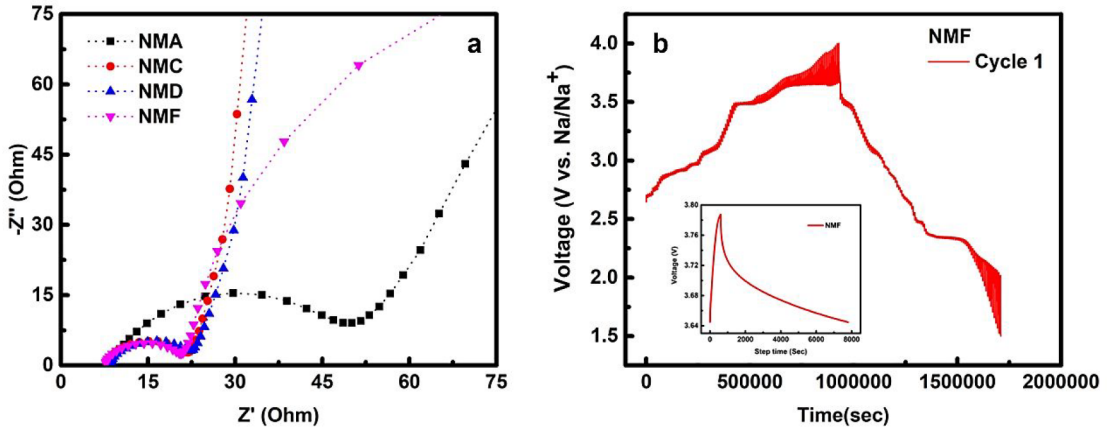

Figure 3. Electrochemical impedance of Na-rich cathodes with different F levels: y = 0.0, 0.2, 0.3, and 0.5 (a). GITT to calculate sodium diffusivity for the NMF sample (b).

Table 1. Calculated Cell Parameter Data Using Rietveld Analysis

	cell parameters				fitting factors				high-intensity peak
F content	a (nm) (±0.005)	b (nm) (±0.007)	c (nm) (±0.002)	β (deg) (±0.03)	R_{wp}	R_{exp}	χ^2	GOF	2θ (deg) (002)
0.000	0.286	0.567	0.580	113.100	1.370	0.980	1.950	1.400	16.584
0.100	0.286	0.567	0.580	113.127	1.460	0.980	2.220	1.490	16.570
0.200	0.286	0.567	0.580	113.136	2.020	0.980	4.250	2.060	16.580
0.300	0.284	0.529	1.115	90.470	1.780	0.920	3.740	1.930	15.781
0.400	0.283	0.525	1.115	90.169	1.910	1.120	2.910	1.710	15.825
0.500	0.284	0.523	1.126	90.200	1.390	1.170	1.560	1.250	15.702

value tends to be highly stable. In our case, it can be noted that with the increase in the F content the peak separation was reduced stepwise from 380 mV for the NMA samples to 250 mV for the NMF samples. This reduction in the redox peak separation value is very well in agreement with the enhanced stability of the NMF samples with a high level of F substitution. Furthermore, it should be noted that unlike in the case of NMA where the major significant redox peaks occurred between 2.67 and 2.29 V, in the case of the NMF samples, various minor but significant redox peaks other than the major peaks at 2.54 and 2.29 V were prominent. Tracing the transition of the F substitution from y = 0 to 0.5, it is observed that these minor peaks become prominent with increasing F content, particularly for NMD, and cause a downshift in the anodic peak from 2.67 V for NMA to 2.54 V for NMF. It is speculated that these peak shifts and minor peaks are associated with the phase transition of the pristine NMA sample due to F substitution. To gain a better insight into these speculations, the samples were further analyzed by various physical methods, including the Rietveld and XAS analyses presented in the following sections.

Fluorine is well-known for increasing the rate performance and the sodium diffusivity by enabling the 0-TM transition in rock salt cathodes. To validate this, electrochemical impedance spectroscopy (EIS) was employed to determine the conductivity of all the samples. As shown in Figure 3a, it can be observed that fluorine significantly improves the conductivity of the samples from 52 Ω for the NMA sample to 18 Ω for the NMF sample. It can also be observed that the difference in resistance among other F-containing samples is less significant. Even after 300 cycles, as shown in Figure S2, the resistance increase due to structural loss is much higher in the NMA sample than in the NMF sample, indicating better structural stability even after cycling. To further analyze the Na diffusivity of the NMF sample, the galvanostatic intermittent titration technique (GITT) was applied with 600 s of charge time and 7200 s of discharge time to attain potential (V) stability. An optimal overpotential was observed, as illustrated in Figures 3b and S9. The Na diffusion coefficient was estimated to be in the range of 10^{-15}–10^{-11} cm^2 s^{-1} for NMF. The unit cell volume was considered for the calculation of diffusivity. It can be noted that the Li diffusion coefficient in a Li-rich oxide cathode is ~10^{-16}–10^{-13} cm^2 s^{-1}.[35] Overall, the addition of fluorine significantly increased the Na-ion diffusivity, making it comparable to that of Li in Li-based layered cathodes. It is observed from the above studies that the substitution of F at the anion site significantly improves the conductivity as well as the cycle stability.

Rietveld Analysis. To obtain insight into fluorine substitution for oxygen and its role in improving the performance of a cathode, the Rietveld analysis was performed on all the samples using Profex software.[36] The Rietveld analysis is a powerful tool that is capable of providing various insights into crystallography, elemental composition, and chemical bonding, for example. Initially, using Rietveld analysis, all the major and minor peaks were resolved into the corresponding phases and planes of $NaMnO_{2-y}F_y$. While resolving the first major peak of all samples, a shift to a lower 2θ was observed with the increase in F content. Correspondingly, changes in other minor peaks were also observed for the NMA through NMF samples. Using the Rietveld analysis, various structural models of $NaMnO_2$ were evaluated to analyze the components present in each sample. It is observed that with the increase in F content from the pristine NMA sample to the NMF sample the cathode material evolves from an O3 type to a P2 type as a result of F substitution. As shown in Table 1, the composition of each phase in each sample explains the evolution of O3-type NMA to P2-type NMF. In

https://doi.org/10.1021/acsaem.2c03391
ACS Appl. Energy Mater. 2023, 6, 960−968

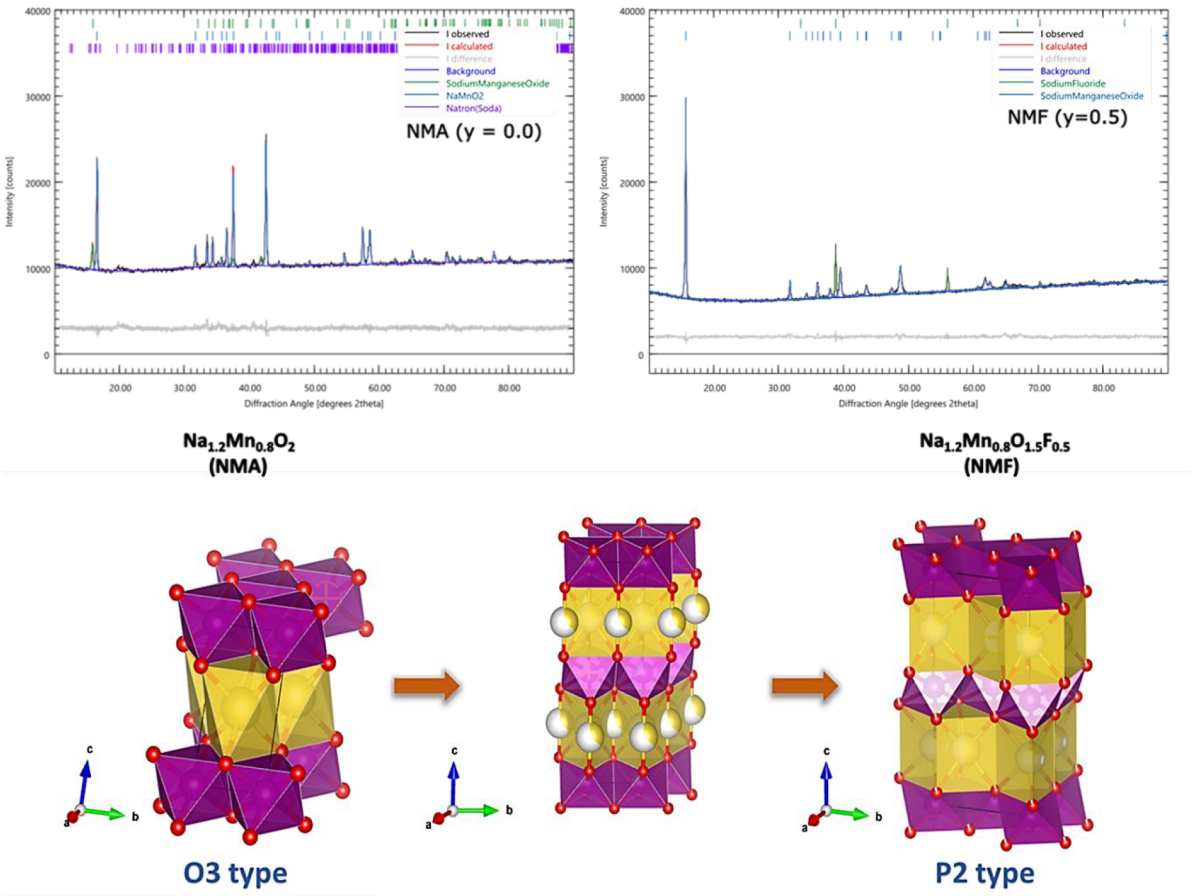

Figure 4. Rietveld analysis of Na-rich cathodes (top). Schematic representing the evolution of the cathode structure upon F substitution and the corresponding effect in the crystal structure (bottom).

Figure S3 it is interesting to note that with the increase in the F content the presence of Na_2CO_3 reduced to zero or negligible, which is in good agreement with the fact that F prefers alkali metals (Na or Li) over transition metals. For each model during the Rietveld analysis, a slight modification at the oxygen anion site was made to the original structure based on the crystallographic data presented in Figures 4, S4, and S5. The relevance of the models to experimental data was well within the agreeable range as demonstrated by various R values, χ^2, and goodness of fit (GOF). Additionally, for each sample, the composition of elements was analyzed using the Rietveld analysis to determine the substitution level of F into pristine $Na_{1.2}Mn_{0.8}O_2$. The values shown in Table S1 are in good agreement with experimental values. With the increase in F content, the oxidation state of Mn^{3+} may have increased to near Mn^{4+}, which leads to the formation of P2-type NMOF materials, as shown in Figure 4. Commonly, these P2-type cathodes require a higher firing temperature and a slower cooling process to obtain the same oxidation state, a feat of which is severely hindered by the formation of many impure phases, according to Kumakura et al.[27] To avoid impurities formed by firing at low temperatures, they adopted a high temperature and reported distorted and undistorted $Na_{0.69}MnO_2$ with the highest purity. Our NMF sample opens a new pathway to achieve distorted $NaMnO_2$ at much lower firing temperatures. It is observed that fluorine increases the oxidation state of Mn from 3+ to almost 4+ and thus avoids impurity formation, as stated by Kumakora et al.,[27] and also causes distortion in the crystal structure as observed in the P′2-type cathode. Therefore, this presents a new strategy for achieving high-purity samples that are highly sensitive to various synthesis environments. To further confirm the changes in the oxidation state of Mn^{3+} and the distortion in the structure and coordination chemistry, X-ray absorption spectroscopy (XAS) analysis was performed on all the samples.

XANES and XAFS Studies. X-ray absorption spectroscopy was used to determine the interim effects of F substitution in a layered cathode sample, particularly at the Mn transition-metal site. XAS is so sensitive that it can detect very subtle changes in the crystallography of a sample. Although other methods, such as XRD Rietveld analysis, allow us to record the changes in the crystal structure, it does not quantify the impact of F substitution. Thus, a comparative study of the XANES spectra of Mn based on F substitution is necessary. The reference XANES spectra at E_0 values of 6548.0, 6556.08, and 6560.09 eV were also recorded for the reference compounds of MnO, Mn_2O_3, and MnO_2, respectively. The entire set of data was analyzed using LARCH software developed by Newville.[37] Using this software and carefully verifying the derivatives, the E_0 values for each sample are listed in Table S2.

Pre-Edge Analysis. In the pre-edge region, due to the partial filling of transition-metal d-shells, the p−d hybridization dramatically changes corresponding to the distortion in the transition-metal octahedra. This is largely evident in the tetrahedral coordination, which results in a sharp pre-edge absorption peak. This sensitivity to the local geometry around the absorbing atom provides greater insights into the coordination chemistry and bonding characteristics. The

https://doi.org/10.1021/acsaem.2c03391
ACS Appl. Energy Mater. 2023, 6, 960−968

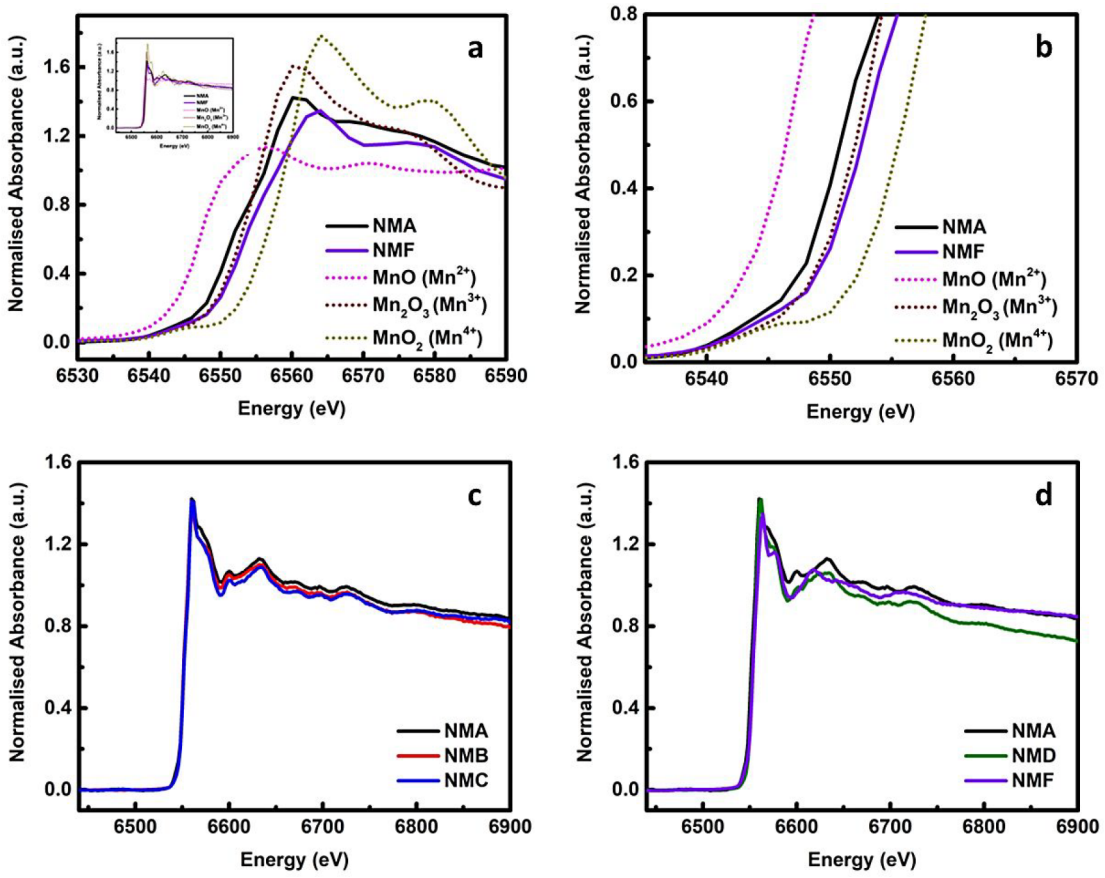

Figure 5. XANES spectra of cathode materials $y = 0$ and 0.5 in reference to standards (a). Formation of the minor peak for the NMF sample at the pre-edge region (b). XANES spectra of cathode materials with $y = 0–0.2$ (c) and $y = 0$, 0.3, and 0.5 (d).

evolution of the pre-edge region in the as-synthesized samples with the increase in F content was studied. As illustrated in Figure 5b, initially, no prominent pre-edge peak is visible for NMA, indicating the presence of perfect octahedra, which is consistent with the Rietveld data of the NMA sample. With the subsequent increase in F substitution, the octahedra of Mn−O become affected, and a peak begins to rise at the pre-edge zone at approximately 6545.0 eV. This distortion further confirms the distorted cell model speculated in the Rietveld analysis.

Edge Analysis. With the change in the coordination chemistry of the Mn−O octahedra, it is highly plausible that the oxidation number of Mn may have been altered. XANES edge spectra are highly sensitive to such changes in the oxidation number and were used to evaluate the oxidation number of Mn in all samples, as shown in Figure 5. In particular, XANES edge spectra can detect the lowest unfilled electronic levels of an absorbing atom as well as its oxidation state and coordination chemistry. To evaluate the average oxidation number of Mn in all the samples, a linear combination fitting method was used and tabulated in Table S2. It is confirmed that the average oxidation number was slightly altered by F substitution with consistent increase in weight of +4 oxidation state from NMA to NMF. With the change in the oxidation number, the bond lengths Mn−O can be altered, and this was successfully evaluated by the Rietveld analysis previously. This confirms the formation of the P′2-type cathode, which is favorably formed by the higher oxidation of the Mn ion. Hence, this phase formation plays a vital role in improving the capacity and multistep GCD process much similar to that of P′2 $Na_{0.67}MnO_2$ reported by Kumakura et al.

EXAFS Analysis. To further analyze the change in Mn−O bonding and to confirm the substitution of F into the Mn−O octahedra, EXAFS analysis was performed in the far-edge spectra. In the far-edge region, i.e., beyond 150 eV after the edge, the absorption $(\mu(E))$ is highly sensitive to the distance and type of neighboring absorbing atoms. Because of the wave nature of photoelectrons, the EXAFS are defined by the oscillations above the absorption edge as a function of the wavenumber (χ) and given as

$$\mu(E) = \mu_0(E)[1 + \chi(E)] \quad (1)$$

$$\chi(E) = \frac{\mu(E) - \mu_0(E)}{\Delta\mu_0(E_0)} \quad (2)$$

The local structure of manganese ions with various levels of F substitutions was measured with EXAFS. By extrapolating the Victoreen-type function with the order of zero, backgrounds were subtracted from the pre-edge region, and cubic spline functions were used for the EXAFS oscillation $\chi(k)$ extraction. Edge jump values were used to normalize the EXAFS spectra. The Fourier transformations of the EXAFS resulted in the pseudoradial structure functions (RSF) for the absorbing manganese (Mn) atom. For a K range of 2.5−10.5 $Å^{-1}$ with K^2 weighting, Fourier transformations were performed with minimal error due to noise. The Mn−Na interaction was minimal because of the low backscattering ability of sodium. Figures S6 and S7 show the Fourier transformations of the

https://doi.org/10.1021/acsaem.2c03391
ACS Appl. Energy Mater. 2023, 6, 960−968

EXAFS oscillation for the Mn K edge of the F-substituted samples compared with the pristine Na-rich cathode. The peak distances obtained may seem smaller due to the absence of phase shift corrections in the FT spectra. Among the various peaks, the first two high-intensity peaks correspond to the Mn−O and Mn−Mn bonding. The simple Fourier-transformed backscattering of the photoelectrons represents six oxygen coordination (partially replaced by fluorine) with the Mn absorbing atom at the first shell followed by Na and Mn at the second shell. The local order is greatly reflected by the coordination number and Debye−Waller factor (σ) in the RSF with peak intensities and broadness.

The local distortion was further estimated quantitatively by curve fitting the FT data and Fourier filtering of the corresponding oxygen, fluorine, and other cation neighbors. By keeping the coordination numbers constant, the interatomic distances d and σ were left as variables in the list of parameters. The interaction distance between the absorbing atom and the first and second shell atoms is in agreement with Shannon's ionic radii. In Figures S6 and S7, the peak intensities and phase of the wave at lower R value (i.e., Mn−O bonding region) for F-substituted $Na_{1.2}Mn_{0.8}O_2$ samples were slightly different compared to those of the pristine samples because of the change in oxidation and distortion in the bonding. On the basis of the increase in σ^2 value of axial Mn−Mn from 0.006 to 0.013 for NMA to NMF, respectively, which is strongly associated with local distortion, it can be further confirmed that considerable distortion in the long-range order (LRO) occurred. Overall, it is learned that F anion substitution induces a distortion in an ordinary layered cathode, and this distortion is a key factor leading to enhanced electrochemical properties of the NMF cathode. Though the exact impact of this distortion in structure is unknown, we shall study and report the same in the future.

CONCLUSION

To keep abreast with recent industrial trends that are more focused on energy materials with superior cyclability at higher current rates for a faster charging process, in this paper, we present F-substituted $Na_{1.2}Mn_{0.8}O_{1.5}F_{0.5}$. The structural integrity of the material is the key factor in enabling superior cyclability of the cathode material, which is achieved by F substitution. In addition, owing to the anion substitution of F for O, few distortions were induced in the cathode, enhancing the capacity of the cathode by reducing the transition-metal valency and significantly increasing the cycle stability by robust structural evolution. In addition to analyzing the cathode performance, the effect of fluorine substitution on the cathode structure and transition-metal valency was systematically studied and analyzed using Rietveld, XANES, and EXAFS analyses. This study includes only the systematic F substitution up to 25% (i.e., $O_{1.5}F_{0.5}$) at an anion site based on previous theoretical studies on lithium counterparts. The superior performance of this class of cathodes paves the way for cathode materials that demonstrate both high capacity and enhanced stability.

ASSOCIATED CONTENT

Supporting Information

The Supporting Information is available free of charge at https://pubs.acs.org/doi/10.1021/acsaem.2c03391.

Tables summarizing the XAS data and cathode performance comparison with earlier reports along with eight supporting figures (PDF)

AUTHOR INFORMATION

Corresponding Author

Yun-Sung Lee − *School of Chemical Engineering, Chonnam National University, Gwangju 61186, Republic of Korea;* orcid.org/0000-0002-6676-2871; Email: leeys@chonnam.ac.kr

Author

Bala Krishnan Ganesan − *School of Chemical Engineering, Chonnam National University, Gwangju 61186, Republic of Korea;* orcid.org/0000-0001-5595-0503

Complete contact information is available at: https://pubs.acs.org/10.1021/acsaem.2c03391

Notes

The authors declare no competing financial interest.

ACKNOWLEDGMENTS

This work was supported by the National Research Foundation of Korea (NRF) grant funded by the Korean government (Ministry of Science, ICT & Future Planning) (No. 2019R1A2C1007620).

REFERENCES

(1) Lee, J.; Wang, C.; Malik, R.; Dong, Y.; Huang, Y.; Seo, D. H.; Li, J. Determining the Criticality of Li-Excess for Disordered-Rocksalt Li-Ion Battery Cathodes. *Adv. Energy Mater.* **2021**, *11* (24), 2100204.

(2) Zhang, X.; Qiao, Y.; Guo, S.; Jiang, K.; Xu, S.; Xu, H.; Wang, P.; He, P.; Zhou, H. Manganese-Based Na-Rich Materials Boost Anionic Redox in High-Performance Layered Cathodes for Sodium-Ion Batteries. *Adv. Mater.* **2019**, *31* (27), No. 1807770.

(3) Mu, L.; Xu, S.; Li, Y.; Hu, Y. S.; Li, H.; Chen, L.; Huang, X. Prototype Sodium-Ion Batteries Using an Air-Stable and Co/Ni-Free O3-Layered Metal Oxide Cathode. *Adv. Mater.* **2015**, *27* (43), 6928−6933.

(4) Thangavel, R.; Moorthy, M.; Ganesan, B. K.; Lee, W.; Yoon, W.; Lee, Y. Nanoengineered Organic Electrodes for Highly Durable and Ultrafast Cycling of Organic Sodium-Ion Batteries. *Small* **2020**, *16* (41), No. 2003688.

(5) Liu, Y.; Li, W.; Xia, Y. Recent Progress in Polyanionic Anode Materials for Li (Na)-Ion Batteries. *Electrochem. Energy Rev.* **2021**, *4* (3), 447−472.

(6) Zhou, Q.; Wang, L.; Li, W.; Zhao, K.; Liu, M.; Wu, Q.; Yang, Y.; He, G.; Parkin, I. P.; Shearing, P. R.; Brett, D. J. L.; Zhang, J.; Sun, X. Sodium Superionic Conductors (NASICONs) as Cathode Materials for Sodium-Ion Batteries. *Electrochem. Energy Rev.* **2021**, *4* (4), 793−823.

(7) Ma, X.; Chen, H.; Ceder, G. Electrochemical Properties of Monoclinic NaMnO2. *J. Electrochem. Soc.* **2011**, *158* (12), A1307.

(8) Sato, T.; Yoshikawa, K.; Zhao, W.; Kobayashi, T.; Rajendra, H. B.; Yonemura, M.; Yabuuchi, N. Efficient Stabilization of Na Storage Reversibility by Ti Integration into O ′ 3-Type NaMnO 2. *Energy Material Advances* **2021**, DOI: 10.34133/2021/9857563.

(9) Ha, K. H.; Woo, S. H.; Mok, D.; Choi, N. S.; Park, Y.; Oh, S. M.; Kim, Y.; Kim, J.; Lee, J.; Nazar, L. F.; Lee, K. T. Na4-AM2+α/2(P2O7)2 (2/3 ≤ α ≤ 7/8, M = Fe, Fe 0.5Mn0.5, Mn): A Promising Sodium Ion Cathode for Na-Ion Batteries. *Adv. Energy Mater.* **2013**, *3* (6), 770−776.

(10) Szymanski, N. J.; Zeng, Y.; Bennett, T.; Patil, S.; Keum, J. K.; Self, E. C.; Bai, J.; Cai, Z.; Giovine, R.; Ouyang, B.; Wang, F.; Bartel, C. J.; Clément, R. J.; Tong, W.; Nanda, J.; Ceder, G. Understanding the Fluorination of Disordered Rocksalt Cathodes through Rational

Exploration of Synthesis Pathways. *Chem. Mater.* **2022**, *34* (15), 7015−7028.
(11) Lun, Z.; Ouyang, B.; Kitchaev, D. A.; Clément, R. J.; Papp, J. K.; Balasubramanian, M.; Tian, Y.; Lei, T.; Shi, T.; McCloskey, B. D.; Lee, J.; Ceder, G. Improved Cycling Performance of Li-Excess Cation-Disordered Cathode Materials upon Fluorine Substitution. *Adv. Energy Mater.* **2019**, *9* (2), 1802959.
(12) Zhang, H.; Song, T. Synthesis and Performance of Fluorine Substituted Li1.05(Ni0.5Mn0.5)0.95O2−xFx Cathode Materials Modified by Surface Coating with FePO4. *Electrochim. Acta* **2013**, *114*, 116−124.
(13) Li, H.; Fan, L. Z. Effects of Fluorine Substitution on the Electrochemical Performance of Layered Li-Excess Nickel Manganese Oxides Cathode Materials for Lithium-Ion Batteries. *Electrochim. Acta* **2013**, *113*, 407−411.
(14) Clément, R. J.; Lun, Z.; Ceder, G. Cation-Disordered Rocksalt Transition Metal Oxides and Oxyfluorides for High Energy Lithium-Ion Cathodes. *Energy Environ. Sci.* **2020**, *13* (2), 345−373.
(15) Ji, H.; Urban, A.; Kitchaev, D. A.; Kwon, D. H.; Artrith, N.; Ophus, C.; Huang, W.; Cai, Z.; Shi, T.; Kim, J. C.; Kim, H.; Ceder, G. Hidden Structural and Chemical Order Controls Lithium Transport in Cation-Disordered Oxides for Rechargeable Batteries. *Nat. Commun.* **2019**, *10* (1), 1−9.
(16) Ji, H.; Kitchaev, D. A.; Lun, Z.; Kim, H.; Foley, E.; Kwon, D. H.; Tian, Y.; Balasubramanian, M.; Bianchini, M.; Cai, Z.; Clément, R. J.; Kim, J. C.; Ceder, G. Computational Investigation and Experimental Realization of Disordered High-Capacity Li-Ion Cathodes Based on Ni Redox. *Chem. Mater.* **2019**, *31* (7), 2431−2442.
(17) Lun, Z.; Ouyang, B.; Clément, R. J.; Kwon, D.-H.; Ceder, G. High-Capacity Mn-Based Cation-Disordered Rocksalt Cathodes. *ECS. Meet. Abstr.* **2020**, *MA2020-01* (2), 187−187.
(18) Li, H.; Fong, R.; Woo, M.; Ahmed, H.; Seo, D. H.; Malik, R.; Lee, J. Toward High-Energy Mn-Based Disordered-Rocksalt Li-Ion Cathodes. *Joule* **2022**, *6* (1), 53−91.
(19) Chen, R.; Ren, S.; Mu, X.; Maawad, E.; Zander, S.; Hempelmann, R.; Hahn, H. High-Performance Low-Temperature Li + Intercalation in Disordered Rock-Salt Li−Cr−V Oxyfluorides. *ChemElectroChem.* **2016**, *3* (6), 892−895.
(20) Twu, N.; Li, X.; Urban, A.; Balasubramanian, M.; Lee, J.; Liu, L.; Ceder, G. Designing New Lithium-Excess Cathode Materials from Percolation Theory: Nanohighways in LixNi2−4 x /3Sbx/3O2. *Nano Lett.* **2015**, *15* (1), 596−602.
(21) Lee, J.; Seo, D. H.; Balasubramanian, M.; Twu, N.; Li, X.; Ceder, G. A New Class of High Capacity Cation-Disordered Oxides for Rechargeable Lithium Batteries: Li−Ni−Ti−Mo Oxides. *Energy Environ. Sci.* **2015**, *8* (11), 3255−3265.
(22) Hoshino, S.; Glushenkov, A. M.; Ichikawa, S.; Ozaki, T.; Inamasu, T.; Yabuuchi, N. Reversible Three-Electron Redox Reaction of Mo3+/Mo6+ for Rechargeable Lithium Batteries. *ACS Energy Lett.* **2017**, *2* (4), 733−738.
(23) Yi, T. F.; Sari, H. M. K.; Li, X.; Wang, F.; Zhu, Y. R.; Hu, J.; Zhang, J.; Li, X. A Review of Niobium Oxides Based Nanocomposites for Lithium-Ion Batteries, Sodium-Ion Batteries and Supercapacitors. *Nano Energy* **2021**, *85*, No. 105955.
(24) Lun, Z.; Ouyang, B.; Kitchaev, D. A.; Clément, R. J.; Papp, J. K.; Balasubramanian, M.; Tian, Y.; Lei, T.; Shi, T.; McCloskey, B. D.; Lee, J.; Ceder, G. Improved Cycling Performance of Li-Excess Cation-Disordered Cathode Materials upon Fluorine Substitution. *Adv. Energy Mater.* **2019**, *9* (2), No. 1802959.
(25) Ménétrier, M.; Bains, J.; Croguennec, L.; Flambard, A.; Bekaert, E.; Jordy, C.; Biensan, P.; Delmas, C. NMR Evidence of LiF Coating Rather than Fluorine Substitution in Li(Ni0.425Mn0.425Co0.15)O2. *J. Solid State Chem.* **2008**, *181* (12), 3303−3307.
(26) Stoyanova, R.; Carlier, D.; Sendova-Vassileva, M.; Yoncheva, M.; Zhecheva, E.; Nihtianova, D.; Delmas, C. Stabilization of Over-Stoichiometric Mn4+ in Layered Na2/3MnO2. *J. Solid State Chem.* **2010**, *183* (6), 1372−1379.
(27) Kumakura, S.; Tahara, Y.; Kubota, K.; Chihara, K.; Komaba, S. Sodium and Manganese Stoichiometry of P2-Type Na 2/3 MnO 2. *Angew. Chemie Int. Ed.* **2016**, *55* (41), 12760−12763.
(28) Parant, J. P.; Olazcuaga, R.; Devalette, M.; Fouassier, C.; Hagenmuller, P. Sur Quelques Nouvelles Phases de Formule NaxMnO2 (x ⩽ 1). *J. Solid State Chem.* **1971**, *3* (1), 1−11.
(29) Mendiboure, A.; Delmas, C.; Hagenmuller, P. Electrochemical Intercalation and Deintercalation of NaxMnO2 Bronzes. *J. Solid State Chem.* **1985**, *57* (3), 323−331.
(30) Yabuuchi, N.; Kajiyama, M.; Iwatate, J.; Nishikawa, H.; Hitomi, S.; Okuyama, R.; Usui, R.; Yamada, Y.; Komaba, S. P2-Type Nax[Fe1/2Mn1/2]O2Made from Earth-Abundant Elements for Rechargeable Na Batteries. *Nat. Mater.* **2012**, *11* (6), 512−517.
(31) Kitchaev, D. A.; Lun, Z.; Richards, W. D.; Ji, H.; Clément, R. J.; Balasubramanian, M.; Kwon, D. H.; Dai, K.; Papp, J. K.; Lei, T.; McCloskey, B. D.; Yang, W.; Lee, J.; Ceder, G. Design Principles for High Transition Metal Capacity in Disordered Rocksalt Li-Ion Cathodes. *Energy Environ. Sci.* **2018**, *11* (8), 2159−2171.
(32) Klinger, M.; Jäger, A. Crystallographic Tool Box (CrysTBox): Automated Tools for Transmission Electron Microscopists and Crystallographers. *urn:issn:1600−5767* **2015**, *48* (6), 2012−2018, DOI: 10.1107/S1600576715017252.
(33) Klinger, M. More Features, More Tools, More CrysTBox. *Journal of Applied Crystallography* **2017**, *50* (4), 1226−1234, DOI: 10.1107/S1600576717006793.
(34) Ouyang, B.; Artrith, N.; Lun, Z.; Jadidi, Z.; Kitchaev, D. A.; Ji, H.; Urban, A.; Ceder, G. Effect of Fluorination on Lithium Transport and Short-Range Order in Disordered-Rocksalt-Type Lithium-Ion Battery Cathodes. *Adv. Energy Mater.* **2020**, *10* (10), No. 1903240.
(35) Chen, S.; Xie, Y.; Chen, W.; Chen, J.; Yang, W.; Zou, H.; Lin, Z. Enhanced Electrochemical Performance of Li-Rich Cathode Materials by Organic Fluorine Doping and Spinel Li1+ XNiyMn2-YO4 Coating. *ACS Sustain. Chem. Eng.* **2020**, *8* (1), 121−128.
(36) Doebelin, N.; Kleeberg, R. Profex: A Graphical User Interface for the Rietveld Refinement Program BGMN. *J. Appl. Crystallogr.* **2015**, *48*, 1573−1580.
(37) Newville, M. Larch: An Analysis Package for XAFS and Related Spectroscopies. *J. Phys. Conf. Ser.* **2013**, *430* (1), No. 012007.